Journal of Environmental Chemical Engineering 11 (2023) 111425

Contents lists available at ScienceDirect

Journal of Environmental Chemical Engineering

journal homepage: www.elsevier.com/locate/jece

Photocatalytic properties and antibacterial mechanisms of microbial-derived ZnS/CuS nanocomposites

Haitao Ma [a,1], Keke Wang [b,1], Qilu Zeng [a], Peihan Li [a], Shiping Lyu [a], Bohan Li [a], Xia Luo [a], Liyue Jiang [a], Min Cao [c], Bing Liao [d,*], Zhongping Qiu [a], Likai Hao [e,f,g,**], Can Wang [a,d,***]

[a] Sichuan Engineering Research Center for Biomimetic Synthesis of Natural Drugs, School of Life Science and Engineering, Southwest Jiaotong University, Chengdu 610031, PR China
[b] Sichuan Academy of Eco-Environmental Sciences, Chengdu 610041, PR China
[c] Department of Urology, Chengdu Third People's Hospital, Affiliated Hospital of Southwest Jiao Tong University, Chengdu 610036, PR China
[d] State Environmental Protection Key Laboratory of Synergetic Control and Joint Remediation for Soil & Water Pollution, Chengdu 610059, PR China
[e] State Key Laboratory of Environmental Geochemistry, Institute of Geochemistry, CAS, Guiyang 550081, PR China
[f] University of Chinese Academy of Sciences, Beijing 100049 PR China
[g] CAS Center for Excellence in Quaternary Science and Global Change, Xi'an 710061, PR China

ARTICLE INFO

Keywords:
Biosynthetic nanocomposites
Metal high-value recycling
Antimicrobial mechanism
Visible light photocatalysis

ABSTRACT

The urgency to combat antibiotic-resistant bacterial infections requires new antibacterial materials and methods. Utilizing *Shewanella onesidensis* metabolism, biological zinc/copper sulfide (bio-ZnS/CuS) composites with excellent visible-light photocatalysis effects and broad-spectrum antibacterial activity were synthesized. During synthesis, over 95% of heavy metal ions were recovered from wastewater through co-precipitation to form metal sulfides. The biocomposite with Zn/Cu ratio at 1/9 (Zn_1S/Cu_9S) showed the best photocatalytic performance. Under visible-light catalysis of Zn_1S/Cu_9S, 98.02 ± 0.13% of methylene blue and 81.74 ± 2.12% of rhodamine B were rapidly removed, while sterilization rates exceeded 99.99% against *Escherichia coli* and 99.98% against *Staphylococcus aureus*. The biocomposite showed a nanostructure with sizes between 5 and 20 nm. Characterizations including X-ray photoelectron spectroscopy, UV-Vis absorption spectra, and photoluminescence spectra proved its excellent visible light response capacity (>400 nm) and energy utilization efficiency. Scavenging experiments demonstrated photogenerated holes and hydrogen peroxide as the major reactive oxygen species (ROS) that induce bacterial death. Toxicological studies revealed that ROS attacked bacterial cells by damaging membranes, inhibiting energy metabolism, breaking the antioxidant defense system, and compromising DNA integrity. This research presents innovative solutions for tackling bacterial infections and heavy metal contamination through the advancement of microbial synthetic functional nanomaterials.

1. Introduction

The escalating incidence of drug-resistant bacterial infections significantly burdens healthcare resources [1], which diminishes the efficacy of traditional antimicrobial treatments, underscoring the need for novel antimicrobial strategies [2]. Recent advancements, including gene engineering, microbiota-modulating therapies, antivirulence approaches, and other technology (e.g., catalytic killing) exhibit promising potential, implying new directions for alternative therapies [3–6]. However, their large-scale deployment is limited by challenges like cost-intensive production, suboptimal stability, potential biotoxicity, or the risk of bacterial resistance re-emergence.

Among the above methods, photocatalysis is a promising and green treatment as it can generate abundant reactive oxygen species (ROS) under light to kill bacteria nonselectively and break down organics (e.g. antibiotics and dyes) without causing microbial resistance [7].

* Corresponding author.
** Corresponding author at: State Key Laboratory of Environmental Geochemistry, Institute of Geochemistry, CAS, Guiyang 550081, PR China.
*** Corresponding author at: Sichuan Engineering Research Center for Biomimetic Synthesis of Natural Drugs, School of Life Science and Engineering, Southwest Jiaotong University, Chengdu 610031, PR China.
E-mail addresses: liaobing17@cdut.edu.cn (B. Liao), haolikai@mail.gyig.ac.cn (L. Hao), wangcan@swjtu.edu.cn (C. Wang).
[1] The first two authors contributed equally to this work and should be considered as co-first authors

https://doi.org/10.1016/j.jece.2023.111425
Received 22 August 2023; Received in revised form 28 October 2023; Accepted 3 November 2023
Available online 5 November 2023

Compared with single photocatalytic materials, composite materials demonstrate great functionality and catalytic efficiency advantages, which have been successfully applied in environmental, energy, and medical fields (e.g., water cleaning, hydrogen generation, and sterilization) [8]. Examples include $Cu_{0.9}Mn_{0.05}Ag_{0.05}O$ [9], $ZnO/SrZnO_2$ [10], ZnO/Co_3O_4 [11], and Cu_2S-CdS [12]. However, their synthesis requires harsh reaction conditions, such as high temperatures and pressures, or the use and production of toxic and dangerous chemicals. Biosynthesis of functional nanomaterials is more appealing as it offers a straightforward, environmentally friendly, and cost-effective solution [13].

The biosynthesis approaches are normally based on bioresources (e.g., plant-based materials or molecules, microorganisms, enzymes, and nuclear acids) [14,15]. Many microorganisms (e.g., *Pseudomonas aeruginosa*) can reduce metal ions (e.g., Ni, Pt, and Fe) to elemental nanoparticles (NPs) with catalytic ability [16]. Inorganic anions (OH^-, CO_3^{2-}, and PO_4^{2-}) can also be bio-converted or reduced to react with metal ions and generate NPs, such as $Pr(OH)_3$, $BaCO_3$, and $SmPO_4$ [17,18]. The process removes metal ions as valuable NPs, which is also significant for metal pollution control. Such NPs can be applied in medical diagnosis and treatment, food testing and packaging, pest control, environmental monitoring, and wastewater treatment [19]. For example, gold NPs (Au-N-LK3) with antimalarial activity were synthesized using *Streptomyces* sp. to treat malaria [20]. Over the past decades, microbes have been used to create nanomaterials because they are safe, fast, cheap, and eco-friendly. Nevertheless, several issues need to be addressed for the wide application of microbial-derived nanomaterials, including the separation and purification from the cell body or metabolites, the in-depth biosynthesizing mechanism, and the large-scale production [21,22].

Among the various bio-NPs, bio-metal sulfide is highly valued because its biosynthesis simultaneously extracts heavy metals and sulfur from wastewater, which not only purifies the water but also recycles metal resources. The resulting metal sulfide NPs have great potential in environmental and healthcare applications [23]. For instance, biosynthesized zinc sulfide (ZnS) NPs have demonstrated potential in photocatalytic degradation of organic pollutants like rhodamine B [24]. The bacterial-derived cadmium sulfide (CdS) NPs were found with anticancer properties [25]. Many prior researches have focused on producing individual nanoparticles, which may be unfeasible and require modifications before applications. Utilizing the various metals in the wastewater simultaneously to generate composites could be a solution. The unique morphology and heterostructures formed between different components can alleviate electron-hole recombination and broaden the solar spectrum by matching bandgaps [26,27]. For example, ZnS/CuS composites produced chemically have been utilized to catalyze water to generate hydrogen under visible light, demonstrating higher efficiencies than pure ZnS and CuS [28]. However, there is a dearth of research on the microbial synthesis of metal sulfide composites (biocomposites) to improve efficiency.

In this study, ZnS and CuS nanocomposites (bio-ZnS/CuS) were synthesized for the first time using *Shewanella oneidensis* MR-4 metabolites with heavy metal-containing wastewater as substrate. The bioprocess recovered metal resources as bio-ZnS/CuS, which showed a high visible light catalytic activity to degrade organics and eliminate pathogens. The material properties, photocatalytic performance, and sterilization mechanism were comprehensively evaluated. Utilizing the microbial metabolites, the products can be easily separated and purified for application. And a larger-scale production could be achieved by manipulating bacterial growth and metabolite accumulation. This study offers a new perspective for designing high-performance photocatalysts. By leveraging the metabolic properties of functional bacteria, this study also paves the way for developing efficient and economical methods for heavy metal recovery and wastewater treatment.

2. Materials and methods

2.1. Biosynthesis of bio-ZnS/CuS NPs

The *Shewanella oneidensis* MR-4 (CICC 25104, NCBI sequence no. NC_008321.1) was obtained from the Institute of Geochemistry, Chinese Academy of Sciences. Before use, it was cultured in Luria-Bertani broth at 30 ℃, 150 rpm for 18 h until the late exponential phase. The cells were harvested by centrifugation (6000 rpm, 4 ℃, 7 min) and then transferred into a sterile HEPES-buffered mineral medium. Then it was incubated anaerobically at 30 °C and 200 rpm for 120 h using 20 mM lactate as an electron donor and sodium thiosulfate as an electron acceptor [29]. After cultivation, the culture was centrifuged (10,000 rpm, 5 min, 4 °C) to obtain a supernatant. 10 mM metal salt solutions with varying ratios of Zn to Cu (0:10, 1:9, 3:7, 5:5, 8:2, 10:0) were added drop by drop to the supernatant (50 mL) under vigorous stirring. The resulting product was washed repeatedly with deionized water and ethanol and then dried in a vacuum oven.

To determine the metal removal efficiency, the concentration of Zn and Cu ions in the supernatant was measured using an atomic absorption spectrometer (PinAAcle900T, USA) [30]. The corresponding medium was used as a control to ensure validity.

2.2. Characterizations

Various characterization techniques were conducted to investigate the product property. X-ray powder diffraction (XRD, Thermo Scientific K-Alpha, USA) was used to analyze the crystal structures, while X-ray photoelectron spectroscopy (XPS, Thermo VG Scientific, ESCALAB 250, USA) was utilized to investigate the valence changes of the constituent elements. Transmission electron microscopy (TEM, JEOL JEM 2100 F, Japan) combined with energy-dispersive X-ray spectroscopy (EDS) was used to study the morphological distribution, lattice edge patterns, and elemental analysis. A physisorption analyzer (Micromeritics ASAP 2460, USA) was also utilized to determine the surface area of the material. UV–visible diffuse reflectance spectroscopy (UV–vis, Shimadzu UV-3600 I Plus, Japan) was used to analyze the optical absorption properties. The edge positions of the conduction band (E_{CB}) and valence band (E_{VB}) of materials were also determined [31]. To determine the energy utilization efficiency, a steady-state/transient fluorescence spectrometer (PL, Edinburgh FLS-980, UK) was employed. Lastly, scanning electron microscopy (SEM, ZEISS GeminiSEM 300, Germany) was used to evaluate the bacteria's morphology change [32,33].

2.3. Photocatalytic property measurement

2.3.1. Photocatalytic performance test

The photo-oxidation activity of the prepared NPs was investigated by organic degradation tests under LED (120 mW/cm^2 and $\lambda > 400$ nm). Methylene blue (MB) and rhodamine B (RhB) were used as targets. First, 10.0 mg of NP powder was dispersed in 50 mL of 20.0 mg/L MB solution and continuously stirred in the dark for 30 min to reach adsorption equilibrium. Then 1.0 mL of H_2O_2 was added to increase efficiency before turning on the light. After a predetermined regular interval, the samples were centrifuged and filtered, and the absorption spectra were recorded using a spectrophotometer (DR-2700, HACH Co., Ltd, USA) to determine the dye concentration. Subsequently, 20 mg of the verified optimum biocomposite, pure ZnS, and CuS were added to 100 mL of 15.0 mg/L RhB to determine the degradation kinetics [34]. The degradation efficiency (*DE*) was determined according to $\%DE = \left[\frac{C_o - Ct}{C_o}\right] \times 100$ with C_0 and Ct represents the initial and time dependent dye concentration, respectively [35]. Kinetic fitting was also conducted according to $In\frac{Ct}{C_o} = -kt$ [10].

2.3.2. Antibacterial assay

Escherichia coli (ATCC 25922) and *Staphylococcus aureus* (ATCC 25923) were used as targets (gram-negative and gram-positive) for antibacterial assay with the bacterial cell concentrations around 1.0×10^7 CFU mL^{-1}. The experimental procedures were identical to the photocatalytic performance test except without H_2O_2. The plate count method was used to determine the bacterial inhibition rate [36].

2.3.3. Photocatalytic sterilization mechanism

Various scavengers were employed to explore the bactericidal impact of extracellular ROS species generated from photocatalysis on the bacteria. In detail, the bacterial solution was supplemented with 10 mM isopropanol, 10 mM $Na_2C_2O_4$, 0.05 mM $K_2Cr_2O_7$, 0.1 mM Fe(II), and 2 mM 4-hydroxy-2,2,6,6-tetramethylpiperidin-1-oxyl (TEMPOL) before the antibacterial assay, to quench hydroxyl radicals (•OH), holes (h^+), electron (e^-), hydrogen peroxide (H_2O_2), and superoxide radicals ($\bullet O^{2-}$), respectively [37,38].

2.4. Pathogen biological response under photocatalysis

2.4.1. Fluorescence microscopy assay and intracellular ROS measurement

The bacteria viability was detected using SYTO 9 (excitation/emission wavelength of 485/500 nm) and propidium iodide (PI) dyes (excitation/emission wavelength of 535/617 nm) under a fluorescence microscope. Intracellular ROS was measured using a fluorescent probe DCFH-DA (2′,7′-dichlorodihydrofluorescein diacetate), which interacted with ROS to generate fluorescence to indicate the amount [39,40].

2.4.2. Bacterial physiological response

Photocatalytic oxidative stress triggers the bacterial cell defense system (antioxidant enzymes), whose collapse leads to membrane sabotage, metabolism abnormality, and DNA damage. Therefore, the activities of superoxide dismutase (SOD), catalase (CAT), peroxidase (POD), and glutathione (GSH) content of the pathogen were determined to reflect the antibiotic response under photocatalysis [41–44]. Malondialdehyde (MDA) and adenosine triphosphate (ATP) content were also determined to reflect damage accumulation and cellular metabolic activity. In the meantime, the genomic DNA from *E. coli* and *S. aureus* was extracted using a DNA extraction kit (Tiangen, China) and subjected to electrophoresis on a 1% (w/v) agarose gel to investigate the genomic integrity under photocatalysis [45].

2.5. Data analysis

The experimental data were evaluated using one-way analysis of variance (ANOVA) based on at least three tests. The mean values and standard deviations were calculated using SPSS 22.0 software (IBM, USA). A significance level of $P < 0.05$ was considered statistically significant, while $P < 0.01$ was defined as highly statistically significant. Graphs were plotted using Origin 2022 software.

3. Results and Discussion

3.1. Dyes degradation by bio-ZnS/CuS

As shown in Fig S1a, the bio-ZnS/CuS, with a Zn: Cu ratio of 1:9, had the highest efficiency in degrading MB (98.02 ± 0.13%). The bio-ZnS/CuS with Zn:Cu ratios of 10:0, 3:7, 5:5, 8:2, and 0:10 had degrading efficiencies of 33.00 ± 3.51%, 88.21 ± 4.22%, 80.50 ± 6.36%, 70.04 ± 3.90%, and 84.21 ± 5.23%, respectively. The blank group also showed a slight removal of MB (26.43 ± 1.24%), which could be due to the light-induced degradation. ZnS showed a similar trend with the blank group, indicating its lack of visible-light photocatalysis capacity. The cycling test (Fig. S1b) indicated that after four cycles of experiments, Zn_1S/Cu_9S maintained excellent photocatalytic activity (MB degradation still exceeded 90%). Hence, Zn_1S/Cu_9S was used for further study. The photodegradation curves of RhB under visible light were shown in Fig. S2a. 73.52 ± 1.51% and 81.74 ± 2.12% of RhB was removed by CuS and Zn_1S/Cu_9S, respectively. ZnS showed no photocatalysis capacity, which was nearly identical to the blank. The kinetic analysis (Fig. S2b) indicated Zn_1S/Cu_9S (0.01429 min^{-1} for RhB and 0.03652 min^{-1} for MB) degraded the pollutants faster than ZnS (0.00002 min^{-1} for RhB and 0.00469 min^{-1} for MB) and CuS (0.01325 min^{-1} for RhB and 0.02390 min^{-1} for MB) following a first-order kinetic, proving the improved capacity.

The zinc content had a significant effect on the photocatalytic activity of the biocomposites due to the interfacial charge transfer mechanism and the unique structure of the samples [28,46]. Although having no response under visible light, the appropriate ZnS component can increase the active sites of ZnS/CuS materials and enhance the photo-oxidation ability. This happens when charges move between semiconductors that are close to each other, creating a type I straddling gap semiconductor heterojunction. It allows excited electrons to move from CuS to the conduction band of ZnS, which reduces electron-hole recombination and facilitates light energy utilization, improving photocatalytic efficiency and degrading performance [47,48].

3.2. Characterization of the photocatalyst

The TEM pictures indicated Zn_1S/Cu_9S contained many CuS and ZnS NPs (Fig. 1a-b and Fig. S3a-b) with a film-forming propensity, probably attributed to the negatively charged microbial extracellular organics (e.g., polysaccharides, proteins, peptides). These organics facilitate heterogeneous nucleation of the inorganic phase while impeding homogeneous nucleation, promoting crystal nucleation and growth [49]. Zn_1S/Cu_9S biocomposite's size was primarily within the range of 5–20 nm (Fig. S3c), and the particles between 20 and 50 nm could be attributed to aggregation. The size of pure bio-CuS and ZnS was between 5 and 15 nm, slightly lower than the composites. Fig. 1c presented the composites synthesized without removing the biomass attached to the cell surface with a similar size to those generated by the supernatant. The phenomenon suggested that the synthesis of bio-composites occurred through the in vitro reaction of metal ions with extracellular secretions.

High-resolution TEM images (Fig. 1d) revealed lattice stripes of 0.15 nm corresponding to the facet spacing of (111) for ZnS, and 0.18 nm, 0.26 nm, and 0.17 nm corresponding to the facet spacing of (006), (110), and (103) for CuS, respectively. EDS analysis (Fig. 1e-i) demonstrated the dark brown product had a preconceived metal:S ratio of approximately 1:1 and a Zn: Cu ratio of around 1:9, which can be produced in larger quantities utilizing bacterial supernatant.

The XRD pattern of Zn_1S/Cu_9S (Fig. 2a) revealed diffraction peaks at (52), (64), (59), (56), and (46) corresponded to the crystal planes of sphalerite (JCPDS, 99–0097) and chalcocite (JCPDS, 99–0037). Biogenerated ZnS and CuS also showed the crystal patterns of sphalerite and chalcocite, respectively (Fig. S3d-e). XPS analysis (Fig. 2b-e) found the bio-composite with electron diffraction peaks at 1022.18 eV and 1045.18 eV corresponded to Zn 2p3/2 and Zn 2p1/2, respectively, indicating Zn^{2+}. The spectra peak at 932.63 eV and 952.42 eV confirmed Cu^{2+} existence [50]. Similar to the previous report [46], the electron diffraction peak around 162 eV was observed, which corresponded with the pattern of sulfur in metal sulfide, indicating the existence of S^{2-}.

A large surface area facilitates photocatalytic processes as it provides more surface active sites for reactant molecules to adsorb. The BET surface areas of CuS, ZnS, and Zn_1S/Cu_9S were 56.1 m^2 g^{-1}, 97.6 m^2 g^{-1}, and 84.5 m^2 g^{-1}, respectively (Table S1) [35,51]. With a similar adsorption pattern, the amount of N_2 adsorbed by Zn_1S/Cu_9S was 4.28–14.16% higher than pure CuS under 0.8–1.0 P/P_0 (Fig. S3h) [52]. The result indicated that the incorporation of ZnS in CuS significantly enhanced its BET area, contributing to the property improvement. Molecular adsorption in all samples increased rapidly with higher relative

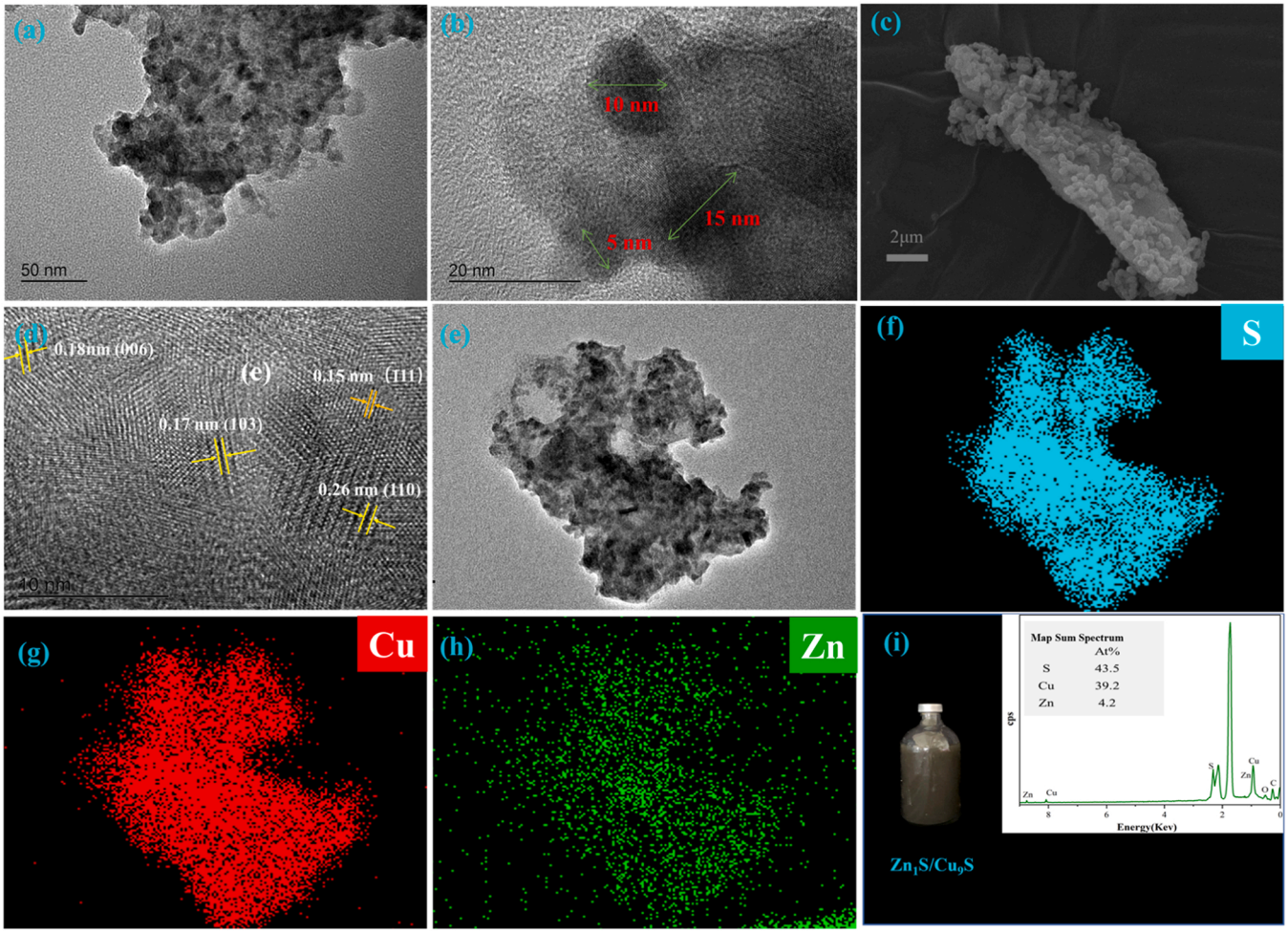

Fig. 1. Micro-structure of the bio-generated material. (a-b) TEM image of Zn_1S/Cu_9S nanoparticles; (c) SEM image of the Zn_1S/Cu_9S on MR-4 cells; (d) HRTEM images of Zn_1S/Cu_9S; (e-h) EDS mapping of Zn_1S/Cu_9S; (i) EDS surface scanning element distribution total spectrum and Bio-CuS, ZnS and ZnS/CuS.

pressures, suggesting the existence of small pores that could be formed by tight aggregation between nanoparticles. The relatively larger pore in Zn_1S/Cu_9S than in ZnS and CuS was probably caused by the more pronounced aggregation (Fig. S3i), which was consistent with TEM results (Fig. 1a).

ZnS absorbs strongly in the UV-Vis spectrum below 350 nm, while Zn_1S/Cu_9S and CuS have similar visible light responses (Fig. 2f). The bandgap of bio-ZnS and CuS is found to be 3.37 eV (E_{VB} of 2.45 eV and E_{CB} of −0.92 eV) and 2.06 eV (E_{VB} of 1.81 eV and E_{CB} of −0.25 eV) (Fig. S2f-g), close to the chemically synthesized ones [28,48]. While the Zn_1S/Cu_9S had a lower bandgap (1.84 eV) (Fig. 2g) [53]. Due to its large bandgap energy, ZnS cannot undergo band-to-band transition under visible light [31,47]. The bio-Zn_1S/Cu_9S had a lower band gap of 1.84 eV compared to both ZnS and CuS (Fig. 2g), which was beneficial for photocatalytic reactions [53]. The Zn_1S/Cu_9S has lower fluorescence intensity than ZnS and CuS (Fig. 2h), suggesting slower electron-hole recombination, higher light energy utilization efficiency, and enhanced photocatalytic activity due to structural differences [54,55].

Based on the above results, the visible light photocatalytic mechanism of CuS/ZnS composites is proposed (Fig. 2i). The composites with ZnS and CuS in close contact facilitate the separation of charge carriers, resulting in significantly enhanced activity compared to pure ZnS or CuS. Moreover, the larger specific surface area of the composites increased the active sites, further contributing to performance enhancement [28,48,56]. The above result confirmed the successful biosynthesis of bio-ZnS/CuS with great visible light catalysis capacity.

3.3. Metal ion removal during biosynthesis

During preparation, Zn^{2+} and Cu^{2+} were removed and recovered as ZnS, CuS, and ZnS/CuS coprecipitates. Post-reaction, over 95% of the metal ions were removed, with or without biomass (Fig. S4). Specifically, when preparing pure CuS and ZnS, 98.3 ± 1.02% of Zn and 97.3 ± 0.81% of Cu were removed. For the bio-ZnS/CuS synthesis with Zn: Cu ratios of 1:9, 3:7, 5:5, and 8:2, the removal efficiency was 98.30 ± 1.31%, 98.80 ± 1.13%, 98.90 ± 0.24%, 97.60 ± 0.35% for Zn and 98.20 ± 1.46%, 97.50 ± 1.65%, 97.30 ± 1.61%, 96.50 ± 0.8% for Cu, respectively.

Metal ions can be adsorbed onto the microbial cell surface and subsequently accumulate within the cells. Moreover, extracellular metabolites can bind or react with metal ions, leading to coprecipitation. In this study, thiosulfate in the medium was enzymatically reduced to S^{2-} and reacted with metal ions to form metal sulfides [55]. The close metal elimination with or without biomass implies that metal removal predominantly relies on sulfide precipitation through cellular metabolism.

3.4. Antibacterial activity and photocatalytic mechanism

Antibacterial assays were performed against *S.aureus* and *E.coli* to determine the sterilizing capacity of the biocomposites (ZnS, CuS, and Zn_1S/Cu_9S) (Fig. 3). Without material addition (control), no obvious inhibition was observed for both bacteria, whether under light or dark (Fig. 3a-b). The bacterial growth was also unaffected by either material under darkness, indicating the requirement of light participation for the

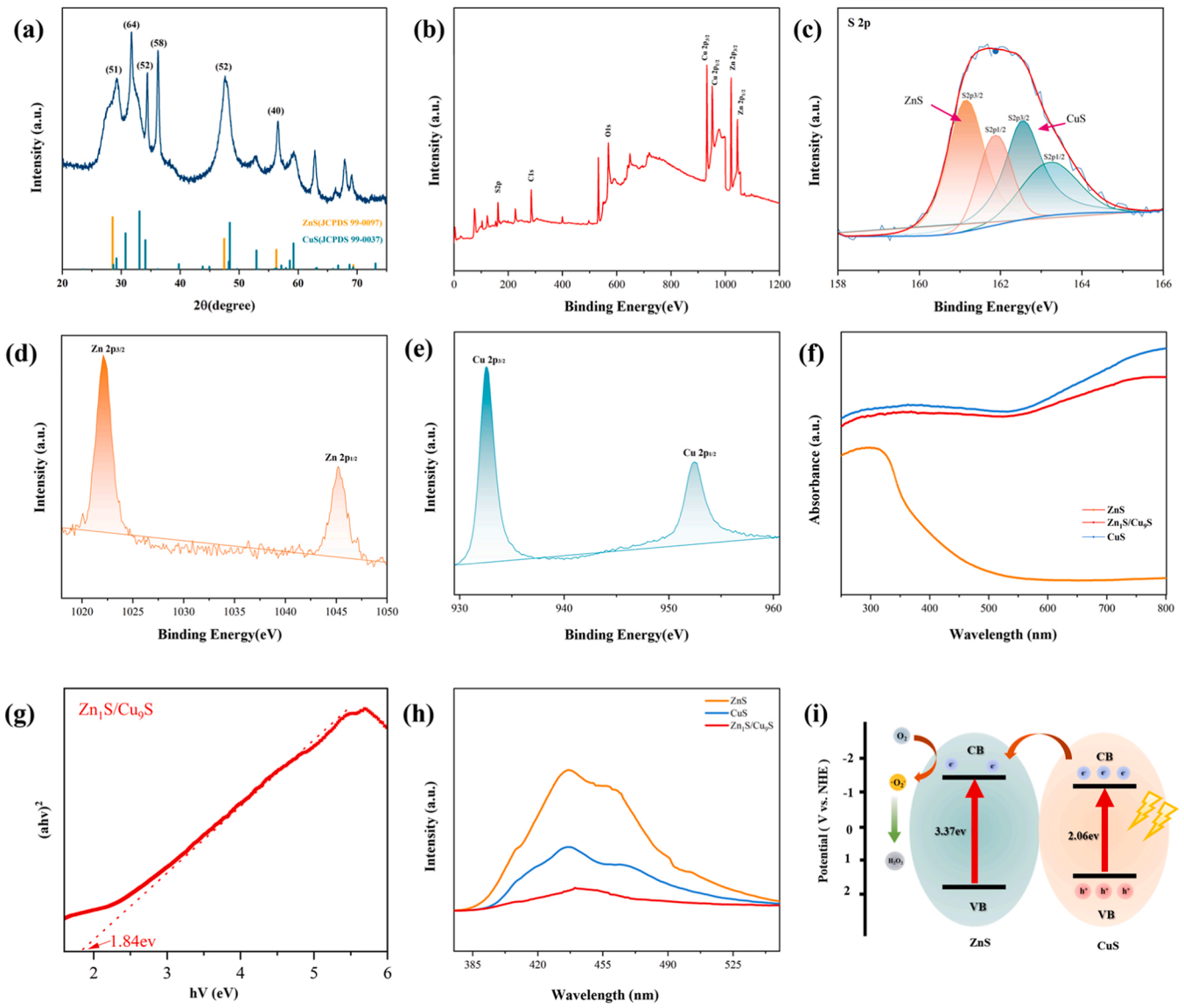

Fig. 2. Characterization of the bio-generated material. (a) XRD spectrum of the Zn_1S/Cu_9S; (b-e) XPS spectrum of the Zn_1S/Cu_9S; (f) UV–vis diffuse reflection spectrum of Zn_1S/Cu_9S; (g) Tauc plots the Zn_1S/Cu_9S; (h) PL excitation spectrum of ZnS, CuS, and Zn_1S/Cu_9S; (i) Photocatalytic mechanism for Zn_1S/Cu_9S photocatalyst.

bactericidal effect. While under visible light, much less colony was observed of Zn_1S/Cu_9S and CuS, indicating their great visible light catalysis capacity. However, no obvious bactericidal effect was found for ZnS, probably due to its limited light response range (Fig. 2f). The bactericidal rate of Zn_1S/Cu_9S reached 99.98% for *S.aureus* and 99.99% for *E.coli*, which was 90.92–92.74% higher than ZnS, and 21.85–16.33% higher than CuS (Fig. S5 and Fig. 3c-d).

Varied scavengers were included to investigate the photocatalytic sterilization mechanism (Fig. 3e-f). Isopropanol, which scavenges ·OH, had no significant impact on the sterilization of *E. coli* and *S. aureus*. The slight inhibitory effect of Cr (VI) and TEMPOL on bacterial inactivation implied that e^- and $\cdot O^{2-}$ played a minor role during bacterial inactivation. Fe(II) and oxalate effectively prevented cell inactivation, indicating H_2O_2 and h^+ as the main ROSs that contributed to the bactericidal process. To sum up, the contribution of ROSs was as follows: $H_2O_2 > h^+ > e^- > \cdot O^{2-} > \cdot OH$.

Zn_1S/Cu_9S showed an optimized optical band position and restricted electron/hole recombination properties compared with pure ZnS or CuS. The migration of electrons from the valence band of CuS to the ZnS surface generates additional electron pairs and reduces O_2 to $\bullet O^{2-}$, then $\bullet O^{2-}$ will continue to be involved in the reaction to produce H_2O_2, thus, the resulting h^+ and H_2O_2 become the main ROSs (Fig. 2i) [10]. The development of heterojunctions between ZnS and CuS allows for the effective separation of charge carriers and results in a substantial increase in the quantity of ROSs (h^+,$\cdot O^{2-}$, e^- and H_2O_2), hence the improved photocatalytic performance [9,57].

3.5. The bacterial response under photocatalysis

3.5.1. Bacterial damage under photocatalysis

MDA content indicates the extent of bacterial lipid peroxidation. Under photocatalysis, a substantial rise in MDA content (Fig. 4a) was observed within the bacterial cells, 88.7% and 78.6% higher than the control for *E. coli* and *S. aureus*, respectively. The result implied that the bacteria underwent substantial lipid peroxidation-induced damage under photocatalytic treatment. ATP levels indicate cellular metabolic activity. As shown in Fig. 4b, the dark-treated groups showed a slightly higher (3.27–4.36%) ATP level than the control (without biocomposite) ($P > 0.05$), probably due to the hormesis effect under metal ions stimulation released from the biocomposite [30,58]. The photocatalytic

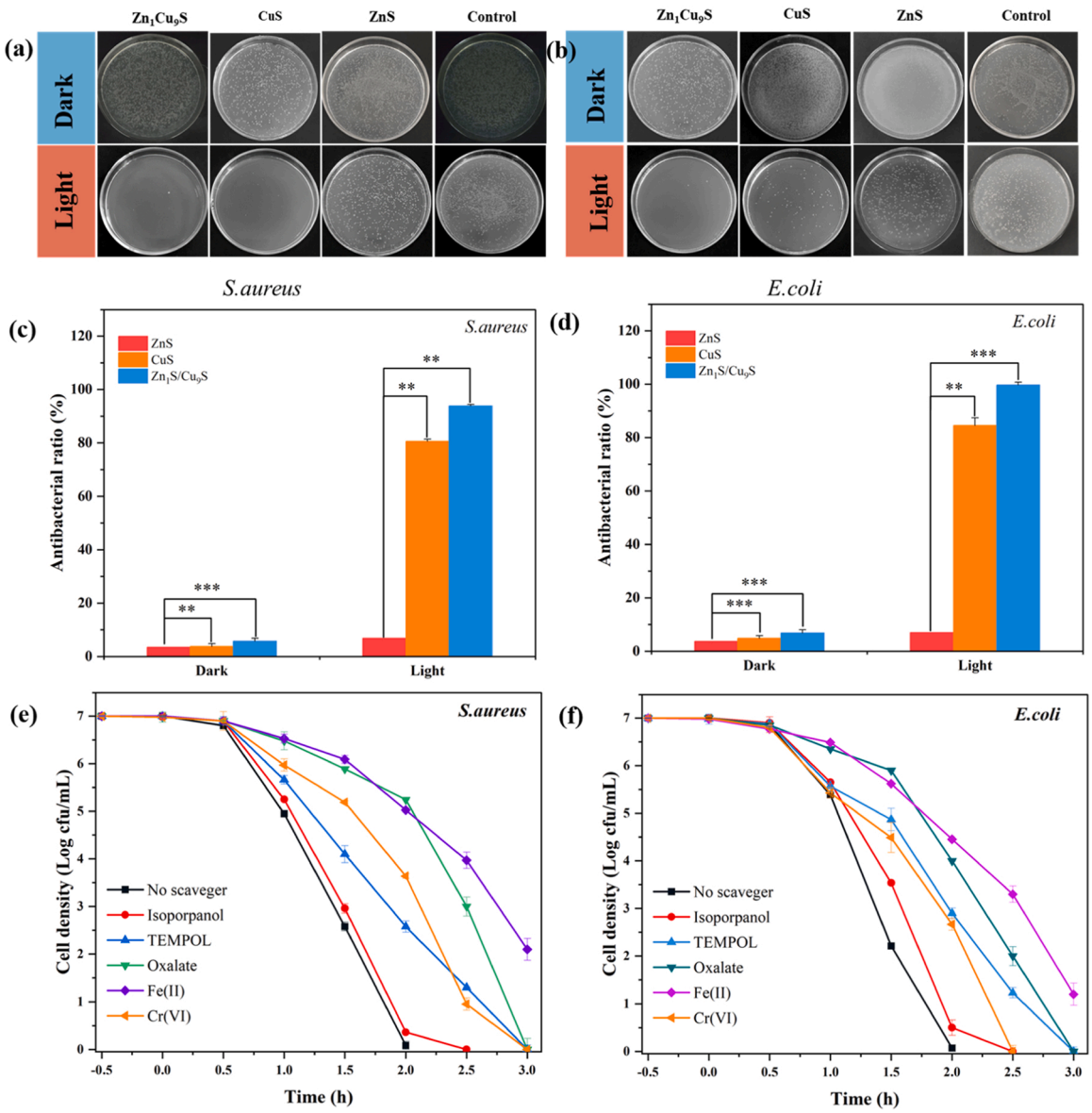

Fig. 3. Response of potential pathogens under photocatalysis of the biogenerated material. (a-b) Spread plate results of *S. aureus* and *E. coli* with different materials; (c-d) Antibacterial activity of different samples against *S. aureus* and *E. coil*, respectively; (e) and (f) Scavenging experiment of photocatalytic inactivation efficiency against *S. aureus* and *E. coli*. Note: "Control" represents the bacteria exposed to visible light. "Dark" represents the bacteria with photocatalytic material in the dark. "Light" indicates that the bacteria are subjected to both the photocatalytic material and visible light simultaneously. Error bars indicate means ± standard deviations: * * $P < 0.05$, and * ** $P < 0.01$.

treatment showed a 63.66% and 55.72% lower ATP level than the control for *E. coli* and *S. aureus*, indicating the greatly inhibited cell metabolism [59].

Intracellular ROS generation was quantified by the fluorescence intensity (Fig. 4c). The much higher fluorescence intensity of *E. coli* and *S. aureus* (167.69% and 147.86%, respectively) under photocatalysis than control ($P < 0.01$) suggested that much more ROS was generated within bacterial cells under photocatalysis (Fig. S6a). Whereas in the absence of light, the relative intensity of fluorescence was close to control. ROS oxidizes the lipid components of the cell membrane, leading to the formation of lipid peroxidation products such as MDA, which affects membrane stability and fluidity. Subsequently, the collapse of the cell membrane leads to membrane organelle structure destruction and, ultimately, cell death [45]. As a gram-negative bacteria, *E. coli* has a thinner cell wall with more lipids than *S. aureus*, causing higher MDA accumulation and fluorescence intensity. The result suggests ROS-induced cell membrane damage could be more severe in gram-negative than gram-positive bacteria [60].

The electrophoresis image (Fig. 4d) revealed that DNA bands in the light-illuminated groups exhibited reduced intensity and clarity, accompanied by pronounced smearing compared to the control. This observation suggests that under photocatalysis, *E. coli* and *S. aureus* experienced significant nucleic acid damage and degradation. The exogenous ROS infiltration and disruption of the internal antioxidant defense system lead to a dramatic increase in intracellular ROS levels and the destruction of intracellular proteins, lipids, and DNA, ultimately leading to cell death [40,45].

Bacterial morphological alterations under photocatalytic stress were illustrated through SEM images (Fig. S6). Normally, *E. coli* exhibited a typical rod-shaped configuration, while *S. aureus* displayed a spherical or ellipsoidal morphology with a smooth surface. Under photocatalytic treatment, a noteworthy augmentation in surface irregularities and roughness, accompanied by cytoplasmic leakage and enhanced cell adhesion, was observed for both bacteria (Fig. S6b). Under fluorescent

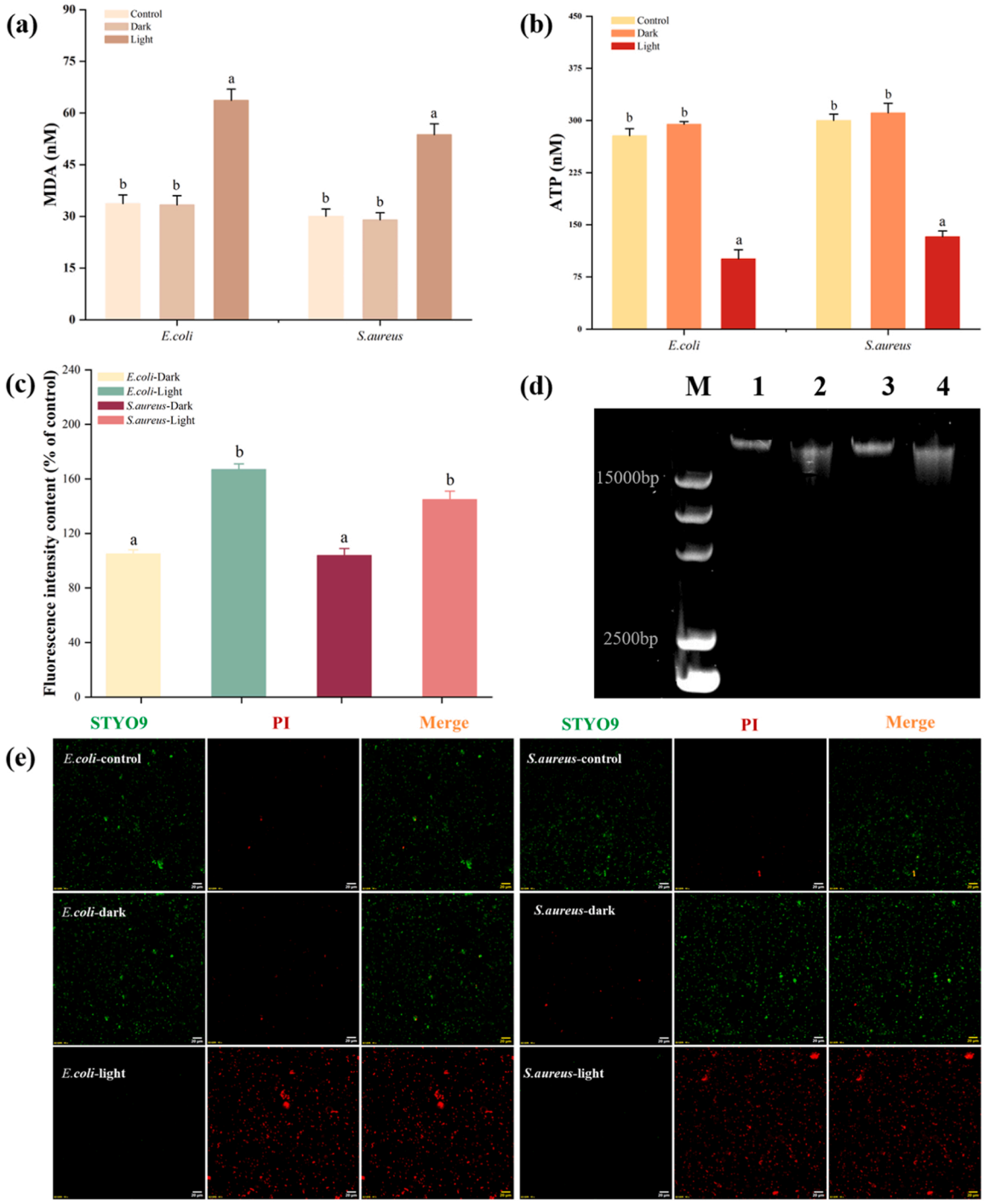

Fig. 4. Bacterial response under photocatalysis. (a) MDA content; (b) ATP content; (c) ROS content by fluorescence intensity; (d) DNA gel electrophoresis: (M) DNA Marker, (1, 3) controls of *E. coli* and *S. aureus*. (2, 4) Light group of *E. coli* and *S. aureus*; (e) live/dead bacteria microscopy. Note: "Control" represents the bacteria exposed to visible light. "Dark" represents the bacteria with photocatalytic material in the dark. "Light" indicates that the bacteria with photocatic material under light. Error bars indicate means ± standard deviations: Different letters indicate $P < 0.05$.

microscopy after dyeing (Fig. 4e), both bacterial cells appeared predominantly green in the control and dark treatment, indicating no severe damage [61]. The little red dots in the dark treatment exhibited slightly toxic effects associated with the nano-size effect and metal ions release (Fig. S7). Under photocatalysis, most cells presented larger red spots, suggesting the death and agglomeration of both bacteria.

3.5.2. Stress response under photocatalysis

In response to stress, antioxidant enzymes (SOD, CAT, and POD) and reducing substances (GSH) are induced to neutralize the radicals and preserve cell viability (Fig. 5a-d). In the dark, enzymatic activity and GSH content remained stable, which aligns with the ROS levels in Fig. 4c, indicating limited oxidative stress. However, under photocatalysis, *E. coli* and *S. aureus* exhibited elevated levels of SOD (23.0 ± 4.56% and 16.02 ± 5.85%), CAT (98.21 ± 11.44% and 35.23 ± 8.71%), and POD (27.11 ± 5.11% and 14.01 ± 7.32%) by 60 min compared to the initial. Nevertheless, the activities of POD and CAT experienced pronounced declines as time progressed, despite the

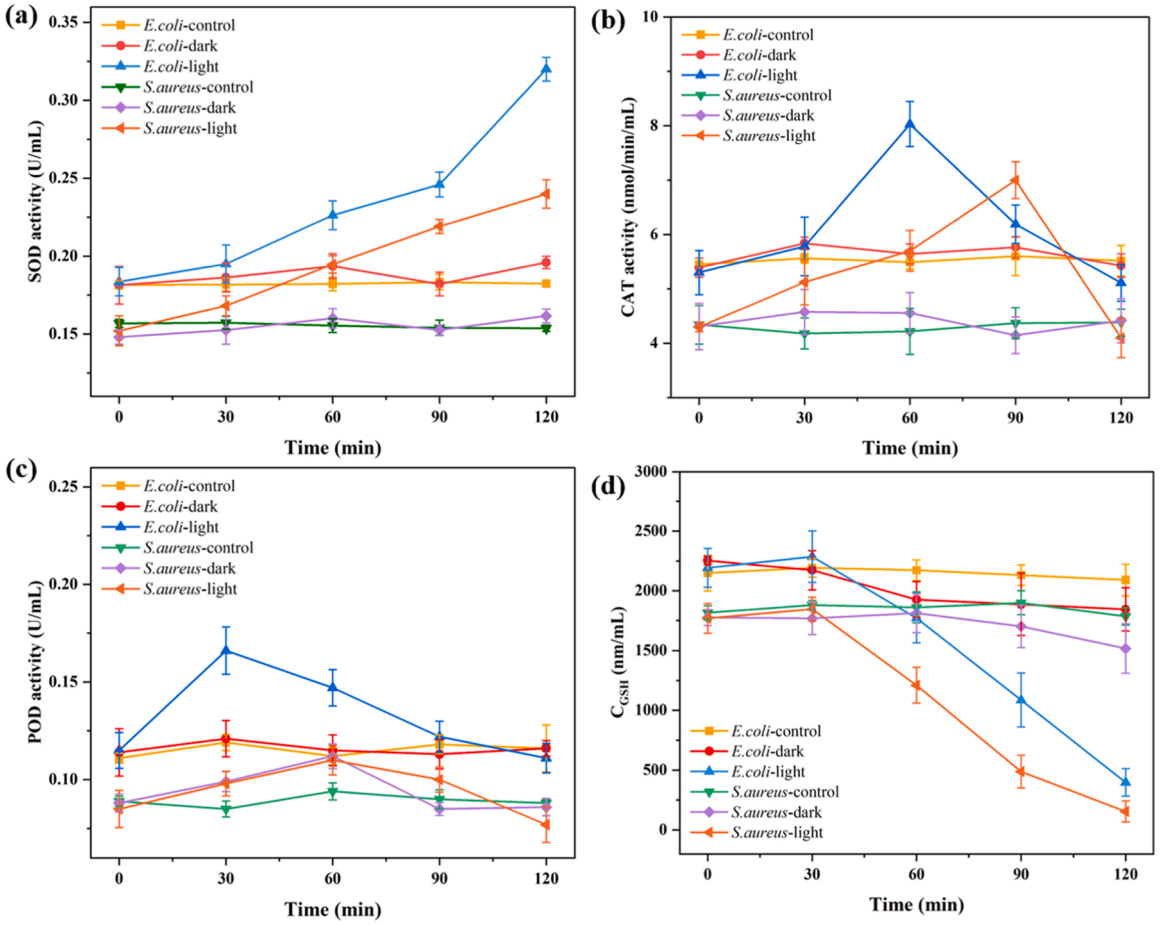

Fig. 5. The activity of SOD (a), CAT (b), POD (c), and GSH (d) of *E. coli* and *S. aureus* under photocatalysis. Note: "Control" represents the bacteria exposed to visible light. "Dark" represents the bacteria with photocatalytic material in the dark. "Light" indicates that the bacteria are subjected to both the photocatalytic material and visible light simultaneously.

continuous elevation in SOD activity. GSH content in both *E. coli* and *S. aureus* initially slightly increased (by 4.33% and 2.21% by 30 min) before declining (81.84% and 91.55% lower by 90 min) compared to the initial.

Under oxidative stress, these enzymes are elevated to eliminate the intracellular ROSs (SOD for $\cdot O^{2-}$, CAT, and POD for H_2O_2) in bacteria and maintain cell homeostasis as the activation of self-protection system [62]. The subsequent decline indicated that ROS accumulation surpassed the enzymes' capacity, resulting in the breakdown of the defense system. SOD is an enzyme that binds to metals and can be activated by various metal ions (Cu, Zn, Fe, and Mn), depending on the specific enzyme type. The trace amount of Zn and Cu ions released from the composite (Fig. S6) could have stimulated the SOD activity and maintained its structure stability under cell damage [63,64]. *E. coli* can produce Cu/Zn-SOD and Mn-SOD while *S. aureus* primarily produces a single-unit Mn-SOD, which potentially elucidates the elevated SOD activity in *E. coli* than *S. aureus* (Fig. 5a) [65,66]. In addition, the relatively stable enzyme structure of SOD allows it to be released into the external environment after bacterial rupture, which could be responsible for the high-level SOD until cell death [67]. GSH is crucial in clearing oxidizing agents and maintaining the cellular redox balance [68]. Under photocatalysis, the GSH levels gradually decreased in both bacteria, indicating the deterioration of bacterial biological functions and, ultimately cell death.

3.6. Future perspective

In the current work, *S. oneidensis* metabolism was employed to recover heavy metals from wastewater and produce functional nanomaterials, which demonstrated commendable visible-light capacity compared with previous results (Table S2). The process showed wide prospects in wastewater treatment, resource recovery, and antimicrobial material development.

During biosynthesis, multiple enzymes are involved in biological sulfur production. In *S. oneidensis*, SirACD can utilize SO_3^{2-}, SO_4^{2-}, or S^0, and PsrABC can use $S_2O_3^{2-}$ or $S_4O_6^{2-}$ as an electron acceptor, as well as degrade cysteine through MdeA, SO_1095, and SseA to produce S^{2-}. The S^{2-} was released to the medium and reacted with metal ions to generate sulfide. The process also occurs on the cell membrane and inside the cell (Fig. 6) [55]. Bacteria such as *Desulfovibrio*, *Desulfococcus*, and *Pseudomonas* also have similar functions [69]. However, some molecular mechanisms need further exploration (e.g., the specific deposition and crystallization process and the interaction mechanisms between bacteria and materials). The process can be further optimized by exploring alternative microbial strains as templates, growth regulation, and feedstock control, which enable greater manipulation of the size, shape, and composition, enhancing the product properties. Such a bioprocess can also be used to treat metal-contaminated wastewater, industrial effluents, or soils, which not only contributes to polluted site remediation but also offers innovative prospects for sustainable resource utilization.

Future research can focus on the molecular interactions between nanocomposites and other clinically relevant bacteria compared to conventional antimicrobial agents. The influence of nanocomposite dose, exposure duration, and environmental factors on bacterial cell viability and death process should also be considered. Furthermore,

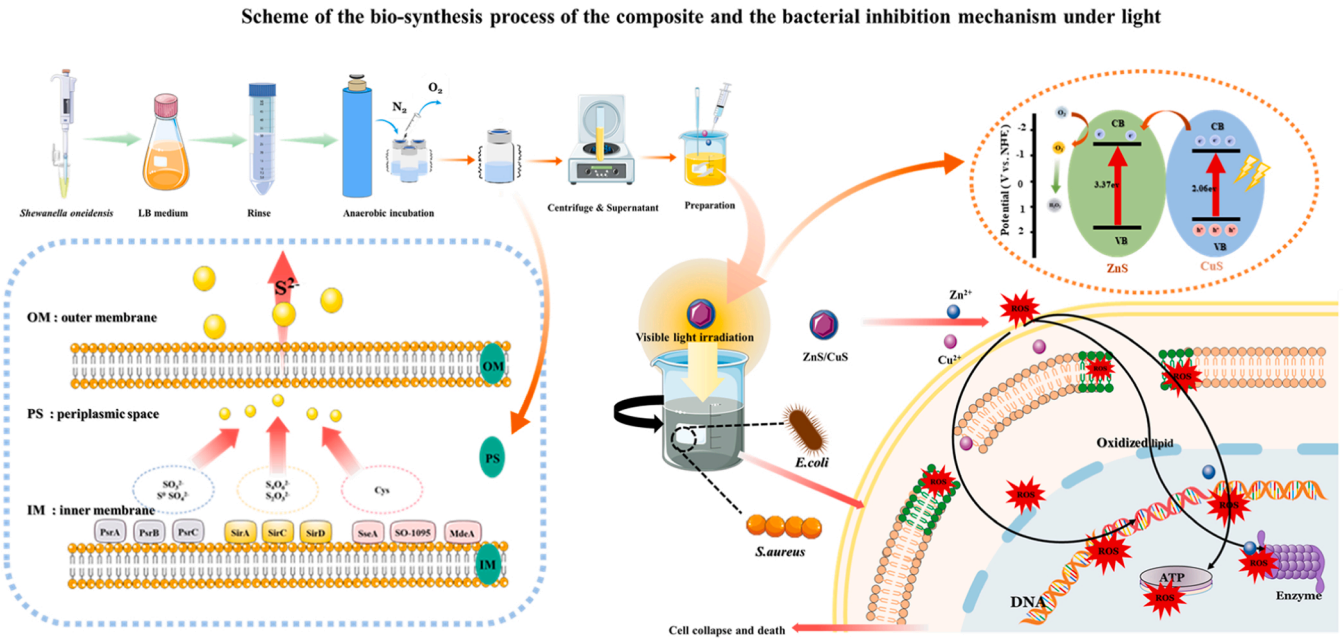

Fig. 6. Scheme of the bio-synthesis process of the composite and the bacterial inhibition mechanism under light.

exploring the potential synergistic effect can offer valuable insights. Further exploration in drug delivery, biosensing, and antimicrobial coatings is also significant for practical implementation.

4. Conclusion

In this paper, microbial metabolism was employed to elucidate the synthesis pathway of ZnS/CuS composites and explore their photocatalytic properties and bacterial inhibition mechanisms. Specifically, the synergistic mechanisms between the composite constituents were comprehensively investigated. The bio-ZnS/CuS can efficiently eliminate organics (MB and RhB) and pathogens (*E. coli* and *S. aureus*) under visible light through photocatalytic oxidation. ROS (mainly h^+ and H_2O_2) generated by the biocomposites effectively deactivate the bacteria by damaging cell walls, membranes, and nucleotides, disrupting energy metabolism and the defense system. The nanostructure and sustained metal ions release also contributed to bacterial death. Our results provide a rational basis for designing and optimizing bio-ZnS/CuS and other biological metal sulfide composites as a photocatalyst for antibiotic substitution and heavy metal recovery.

CRediT authorship contribution statement

Haitao Ma: Conceptualization, Investigation, and Writing. **Keke Wang:** Investigation, Visualization. **Qilu Zeng:** Investigation, Visualization. **Peihan Li:** Investigation, Visualization. **Shiping Lyu:** Editing. **Bohan Li:** Writing – review & editing. **Xia Luo:** Writing – review & editing. **Liyue Jiang:** Writing – review & editing. **Min Cao:** Writing – review & editing. **Bing Liao:** Writing – review & editing. **Zhongping Qiu:** Writing – review & editing. **Likai Hao:** Writing – review & editing. **Can Wang:** Funding acquisition, Supervision.

Declaration of Competing Interest

The authors declare that they have no known competing financial interests or personal relationships that could have appeared to influence the work reported in this paper.

Data Availability

Data will be made available on request.

Acknowledgments

This work was financially supported by the China Postdoctoral Science Foundation (2022M712630), and the opening fund of the State Key Laboratory of Collaborative Control and Joint Remediation of Soil and Water Pollution (GHBK-2021-001), the Fundamental Research Funds for the Central Universities (2682023ZTPY079), Sichuan Administration of TCM Program (2023MS372), the Key Research and Development Plan of Sichuan Province (2023YFSY0011, 2023ZHCG0058), Startup Funding of the Chinese Academy of Sciences (2017-020), National Key Research and Development Project of China (2018YFC1802601), Strategic Priority Research Program of Chinese Academy of Sciences (XDB40020300), and the Large instrument and equipment open test fund of Southwest Jiaotong University (2022SRII-51). We thank Dr. Weizhen Fang of the Analysis & Testing Center, Southwest Jiaotong University, for the technical support.

Appendix A. Supporting information

Supplementary data associated with this article can be found in the online version at doi:10.1016/j.jece.2023.111425.

References

[1] A.H. Holmes, L.S.P. Moore, A. Sundsfjord, M. Steinbakk, S. Regmi, A. Karkey, P. J. Guerin, L.J.V. Piddock, Understanding the mechanisms and drivers of antimicrobial resistance, Lancet 387 (2016) 176–187.
[2] C.D. Fjell, J.A. Hiss, R.E.W. Hancock, G. Schneider, Designing antimicrobial peptides: form follows function, Nat. Rev. Drug Discov. 11 (2012) 37–51.
[3] U. Theuretzbacher, K. Outterson, A. Engel, A. Karlén, The global preclinical antibacterial pipeline, Nat. Rev. Microbiol. 18 (2020) 275–285.
[4] M.A. Harris, K.E. Beenken, M.S. Smeltzer, W.O. Haggard, J.A. Jennings, Phosphatidylcholine Coatings Deliver Local Antimicrobials and Reduce Infection in a Murine Model: A Preliminary Study, Clin. Orthop. Relat. Research® 475 (2017) 1847–1853.
[5] C. Ghosh, P. Sarkar, R. Issa, J. Haldar, Alternatives to conventional antibiotics in the era of antimicrobial resistance, Trends Microbiol. 27 (2019) 323–338.
[6] J.M. Stokes, K. Yang, K. Swanson, W. Jin, A. Cubillos-Ruiz, N.M. Donghia, C. R. MacNair, S. French, L.A. Carfrae, Z. Bloom-Ackermann, V.M. Tran, A. Chiappino-Pepe, A.H. Badran, I.W. Andrews, E.J. Chory, G.M. Church, E.

D. Brown, T.S. Jaakkola, R. Barzilay, J.J. Collins, A deep learning approach to antibiotic discovery, Cell 180 (2020) 688–702, e613.
[7] X. Kong, X. Liu, Y. Zheng, P.K. Chu, Y. Zhang, S. Wu, Graphitic carbon nitride-based materials for photocatalytic antibacterial application, Mater. Sci. Eng.: R: Rep. 145 (2021), 100610.
[8] M. Cai, R. Li, Z. Xie, J. Huang, Y. Zeng, Q. Zhang, H. Liu, W. Lv, G. Liu, Synthesis of a core-shell heterostructured MoS2/Cd0.9Zn0.1S photocatalyst for the degradation of diclofenac under visible light, Appl. Catal. B: Environ. 259 (2019), 118033.
[9] M. Aadil, A. Rahman, S. Zulfiqar, I.A. Alsafari, M. Shahid, I. Shakir, P.O. Agboola, S. Haider, M.F. Warsi, Facile synthesis of binary metal substituted copper oxide as a solar light driven photocatalyst and antibacterial substitute, Adv. Powder Technol. 32 (2021) 940–950.
[10] S. Ahmad, M. Aadil, S.R. Ejaz, M.U. Akhtar, H. Noor, S. Haider, I.A. Alsafari, G. Yasmin, Sol-gel synthesis of nanostructured ZnO/SrZnO2 with boosted antibacterial and photocatalytic activity, Ceram. Int. 48 (2022) 2394–2405.
[11] H.T. Mohammed, K. Kadhim Alasedi, R. Ruyid, S. Abed Hussein, A. Latif Jarallah, S.M.A. Dahesh, M.Q. Sultan, Z.N. Salman, B.S. Bashar, A. Kareem Obaid Aldulaimi, M.A. Obaid, ZnO/Co3O4 nanocomposites: novel preparation, characterization, and their performance toward removal of antibiotics from wastewater, J. Nanostruct. 12 (2022) 503–509.
[12] B. Sadtler, D.O. Demchenko, H. Zheng, S.M. Hughes, M.G. Merkle, U. Dahmen, L.-W. Wang, A.P. Alivisatos, Selective facet reactivity during cation exchange in cadmium sulfide nanorods, J. Am. Chem. Soc. 131 (2009) 5285–5293.
[13] L. Zou, F. Zhu, Z.-e Long, Y. Huang, Bacterial extracellular electron transfer: a powerful route to the green biosynthesis of inorganic nanomaterials for multifunctional applications, J. Nanobiotechnol. 19 (2021) 120.
[14] S. He, L. Zhong, J. Duan, Y. Feng, B. Yang, L. Yang, Bioremediation of wastewater by iron oxide-biochar nanocomposites loaded with photosynthetic bacteria, Front. Microbiol. 8 (2017) 823.
[15] A. Rana, K. Yadav, S. Jagadevan, A comprehensive review on green synthesis of nature-inspired metal nanoparticles: Mechanism, application and toxicity, J. Clean. Prod. 272 (2020), 122880.
[16] S.K. Srivastava, M. Constanti, Room temperature biogenic synthesis of multiple nanoparticles (Ag, Pd, Fe, Rh, Ni, Ru, Pt, Co, and Li) by Pseudomonas aeruginosa SM1, J. Nanopart. Res. 14 (2012) 831.
[17] Y. Choi, T.J. Park, D.C. Lee, S.Y. Lee, Recombinant Escherichia coli as a biofactory for various single- and multi-element nanomaterials, Proceedings of the National Academy of Sciences, 115 (2018) 5944–5949.
[18] M. Jiang, T. Ohnuki, S. Utsunomiya, Biomineralization of middle rare earth element samarium in yeast and bacteria systems, Geomicrobiol. J. 35 (2018) 375–384.
[19] Y. Choi, S.Y. Lee, Biosynthesis of inorganic nanomaterials using microbial cells and bacteriophages, Nat. Rev. Chem. 4 (2020) 638–656.
[20] L. Karthik, G. Kumar, T. Keswani, A. Bhattacharyya, B.P. Reddy, K.V.B. Rao, Marine actinobacterial mediated gold nanoparticles synthesis and their antimalarial activity, Nanomed.: Nanotechnol., Biol. Med. 9 (2013) 951–960.
[21] M. Ramezani Farani, M. Farsadrooh, I. Zare, A. Gholami, O. Akhavan, Green synthesis of magnesium oxide nanoparticles and nanocomposites for photocatalytic antimicrobial, antibiofilm and antifungal applications, Catalysts (2023).
[22] Y. Yang, G.I.N. Waterhouse, Y. Chen, D. Sun-Waterhouse, D. Li, Microbial-enabled green biosynthesis of nanomaterials: current status and future prospects, Biotechnol. Adv. 55 (2022), 107914.
[23] Z. Su, X. Li, Y. Xi, T. Xie, Y. Liu, B. Liu, H. Liu, W. Xu, C. Zhang, Microbe-mediated transformation of metal sulfides: Mechanisms and environmental significance, Sci. Total Environ. 825 (2022), 153767.
[24] X. Xiao, X.-B. Ma, H. Yuan, P.-C. Liu, Y.-B. Lei, H. Xu, D.-L. Du, J.-F. Sun, Y.-J. Feng, Photocatalytic properties of zinc sulfide nanocrystals biofabricated by metal-reducing bacterium Shewanella oneidensis MR-1, J. Hazard. Mater. 288 (2015) 134–139.
[25] L. Wang, S. Chen, Y. Ding, Q. Zhu, N. Zhang, S. Yu, Biofabrication of morphology improved cadmium sulfide nanoparticles using Shewanella oneidensis bacterial cells and ionic liquid: For toxicity against brain cancer cell lines, J. Photochem. Photobiol. B: Biol. 178 (2018) 424–427.
[26] T. Chen, D. Yin, X. Zhang, F. Zhao, K.K. Khaing, L. Deng, K. Huang, L. Li, J. Liu, Y. Zhang, Fabrication of a novel carbon quantum Dots-Modified 2D heterojunction for highly efficient sunlight photocatalysis, J. Alloy. Compd. 806 (2019) 761–773.
[27] Y. Gong, J. Lin, X. Wang, G. Shi, S. Lei, Z. Lin, X. Zou, G. Ye, R. Vajtai, B. I. Yakobson, H. Terrones, M. Terrones, Beng K. Tay, J. Lou, S.T. Pantelides, Z. Liu, W. Zhou, P.M. Ajayan, Vertical and in-plane heterostructures from WS2/MoS2 monolayers, Nat. Mater. 13 (2014) 1135–1142.
[28] J. Zhang, J. Yu, Y. Zhang, Q. Li, J.R. Gong, Visible light photocatalytic H_2-production activity of CuS/ZnS porous nanosheets based on photoinduced interfacial charge transfer, Nano Lett. 11 (2011) 4774–4779.
[29] N.-Q. Zhou, L.-J. Tian, Y.-C. Wang, D.-B. Li, P.-P. Li, X. Zhang, H.-Q. Yu, Extracellular biosynthesis of copper sulfide nanoparticles by Shewanella oneidensis MR-1 as a photothermal agent, Enzym. Microb. Technol. 95 (2016) 230–235.
[30] C. Wang, Y. Jia, J. Li, P. Li, Y. Wang, F. Yan, M. Wu, W. Fang, F. Xu, Z. Qiu, Influence of microbial augmentation on contaminated manure composting: metal immobilization, matter transformation, and bacterial response, J. Hazard. Mater. 441 (2023), 129762.
[31] J. Yu, J. Ran, Facile preparation and enhanced photocatalytic H2-production activity of Cu(OH)2 cluster modified TiO2, Energy Environ. Sci. 4 (2011) 1364–1371.
[32] J. Li, B. Wu, Z. Luo, N. Lei, H. Kuang, Z. Li, Immobilization of cadmium by mercapto-functionalized palygorskite under stimulated acid rain: Stability performance and micro-ecological response, Environ. Pollut. 306 (2022), 119400.
[33] B. Wu, J. Li, H. Kuang, Y. Shangguan, J. Chen, Mercapto-based palygorskite modified soil micro-biology and reduced the uptake of heavy metals by Salvia miltiorrhiza in cadmium and lead co-contaminated soil, J. Environ. Manag. 345 (2023), 118859.
[34] Q. Zhong, H. Lan, M. Zhang, H. Zhu, M. Bu, Preparation of heterostructure g-C3N4/ZnO nanorods for high photocatalytic activity on different pollutants (MB, RhB, Cr(VI) and eosin, Ceram. Int. 46 (2020) 12192–12199.
[35] T. Kousar, M. Aadil, S. Zulfiqar, H.H. Somaily, W. Hassan, H. Sabeeh, F. Mahmood, Temperature controlled synthesis of Co-Ni mixed ferrite nanostructure for the mineralization of azo dye: A novel and facile approach, J. Alloy. Compd. 923 (2022), 166224.
[36] Y. Zhang, C. Wang, R. Yin, A. Cai, X. Yuan, H. Kang, H. Guo, H. Yin, AgNPs as efficient co-catalysts significantly improve the photocatalytic and antibacterial activities of NaTaO3 nanofilms, Mater. Sci. Semicond. Process. 166 (2023), 107738.
[37] J. Luo, H. Han, J. Wu, X. Wang, J. Feng, S. Toan, L. Wang, Y. Lai, Excellent photocatalytic activity of MoO3-adorned g-C3N4 systems: construction of S-scheme heterojunction, Appl. Surf. Sci. 604 (2022), 154512.
[38] Q. Peng, S. Liu, Y. Mao, X. Liu, Preparation of ZnCo2O4/BiVO4 Z-Scheme heterostructures to enhance photocatalytic performance in organic pollutant and antibiotic removal, Colloids Surf. A: Physicochem. Eng. Asp. 655 (2022), 130165.
[39] Y. Lu, L. Li, Z. Lin, L. Wang, L. Lin, M. Li, Y. Zhang, Q. Yin, Q. Li, H. Xia, A new treatment modality for rheumatoid arthritis: combined photothermal and photodynamic therapy using Cu7.2S4 nanoparticles, Adv. Healthc. Mater. 7 (2018) 1800013.
[40] W. Wang, B. Li, H. Yang, Z. Lin, L. Chen, Z. Li, J. Ge, T. Zhang, H. Xia, L. Li, Y. Lu, Efficient elimination of multidrug-resistant bacteria using copper sulfide nanozymes anchored to graphene oxide nanosheets, Nano Res. 13 (2020) 2156–2164.
[41] X. Chen, H. Yin, G. Li, W. Wang, P.K. Wong, H. Zhao, T. An, Antibiotic-resistance gene transfer in antibiotic-resistance bacteria under different light irradiation: Implications from oxidative stress and gene expression, Water Res. 149 (2019) 282–291.
[42] Y. Liang, C. Jiao, L. Pan, T. Zhao, J. Liang, J. Xiong, S. Wang, H. Zhu, G. Chen, L. Lu, H. Song, Q. Yang, Q. Zhou, Degradation of chlorine dioxide bleaching wastewater and response of bacterial community in the intimately coupled system of visible-light photocatalysis and biodegradation, Environ. Res. 195 (2021), 110840.
[43] H. Zhao, X. Guan, F. Zhang, Y. Huang, D. Xia, L. Hu, X. Ji, R. Yin, C. He, Rational design of a bismuth oxyiodide (Bi/BiO1-xI) catalyst for synergistic photothermal and photocatalytic inactivation of pathogenic bacteria in water, J. Mater. Sci. Technol. 100 (2022) 110–119.
[44] B. Wu, J. Li, M. Sheng, H. Peng, D. Peng, H. Xu, The application of biochar and oyster shell reduced cadmium uptake by crops and modified soil fertility and enzyme activities in contaminated soil, SOIL 8 (2022) 409–419.
[45] G. Guan, L. Zhang, J. Zhu, H. Wu, W. Li, Q. Sun, Antibacterial properties and mechanism of biopolymer-based films functionalized by CuO/ZnO nanoparticles against Escherichia coli and Staphylococcus aureus, J. Hazard. Mater. 402 (2021), 123542.
[46] T. Zhu, C.K. Nuo Peh, M. Hong, G.W. Ho, Outside-in recrystallization of ZnS-Cu1.8 S hollow spheres with interdispersed lattices for enhanced visible light solar hydrogen generation, Chemistry 20 (2014) 11505–11510.
[47] Y.P. Xie, Z.B. Yu, G. Liu, X.L. Ma, H.-M. Cheng, CdS-mesoporous ZnS core-shell particles for efficient and stable photocatalytic hydrogen evolution under visible light, Energy Environ. Sci. 7 (2014) 1895–1901.
[48] N. Nwaji, E.M. Akinoglu, Synthesis of ZnS-CuS-Bi nanonail heterostructures and funnel mechanism of their photocatalytic activity, J. Environ. Chem. Eng. 9 (2021), 106066.
[49] J.M. Taylor, A. Konda, S.A. Morin, Spatiotemporal control of calcium carbonate nucleation using mechanical deformations of elastic surfaces, Soft Matter 16 (2020) 6038–6043.
[50] P. Kumar, R. Nagarajan, R. Sarangi, Quantitative X-ray Absorption and Emission Spectroscopies: Electronic Structure Elucidation of Cu(2)S and CuS, J. Mater. Chem. C. 1 (2013) 2448–2454.
[51] M.U. Khalid, K.M. Katubi, S. Zulfiqar, Z.A. Alrowaili, M. Aadil, M.S. Al-Buriahi, M. Shahid, M.F. Warsi, Boosting the electrochemical activities of MnO2 for next-generation supercapacitor application: Adaptation of multiple approaches, Fuel 343 (2023), 127946.
[52] G. Nazik, M. Aadil, S. Zulfiqar, W. Hassan, A. Rahman, S.M. Ibrahim, K. Naseem, T. A. Sheikh, M.N. Akhtar, Synthesis of doped metal sulfide nanoparticles and their graphene reinforced nanohybrid for Pb(II) detection, 237 (2023) 1257–1285.
[53] P.S. Kumar, S. Lakshmi Prabavathi, P. Indurani, S. Karuthapandian, V. Muthuraj, Light assisted synthesis of hierarchically structured Cu/CdS nanorods with superior photocatalytic activity, stability and photocatalytic mechanism, Sep. Purif. Technol. 172 (2017) 192–201.
[54] Y.-M. Hao, S.-Y. Lou, S.-M. Zhou, R.-J. Yuan, G.-Y. Zhu, N. Li, Structural, optical, and magnetic studies of manganese-doped zinc oxide hierarchical microspheres by self-assembly of nanoparticles, Nanoscale Res. Lett. 7 (2012) 100.
[55] Y. Wang, H. Qiu, H. Niu, H. Liu, J. Liu, Y. Jia, H. Ma, F. Xu, L. Hao, Z. Qiu, C. Wang, Effect and mechanism of simultaneous cadmium-tetracycline removal by a self-assembled microbial-photocatalytic coupling system, J. Hazard. Mater. 449 (2023), 131018.
[56] S. Fu, W. Yuan, Y. Yan, H. Liu, X. Shi, F. Zhao, J. Zhou, Highly efficient visible-light photoactivity of Z-scheme MoS2/Ag2CO3 photocatalysts for organic pollutants degradation and bacterial inactivation, J. Environ. Manag. 252 (2019), 109654.

[57] M. Aadil, M. Mahmood, M.F. Warsi, I.A. Alsafari, S. Zulfiqar, M. Shahid, Fabrication of MnO2 nanowires and their nanohybrid with flat conductive matrix for the treatment of industrial effluents, FlatChem 30 (2021), 100316.
[58] C. Wang, Y. Jia, Q. Wang, F. Yan, M. Wu, X. Li, W. Fang, F. Xu, H. Liu, Z. Qiu, Responsive change of crop-specific soil bacterial community to cadmium in farmlands surrounding mine area of Southeast China, Environ. Res. 214 (2022), 113748.
[59] Y. Pu, Y. Li, X. Jin, T. Tian, Q. Ma, Z. Zhao, S.Y. Lin, Z. Chen, B. Li, G. Yao, M. C. Leake, C.J. Lo, F. Bai, ATP-Dependent Dynamic Protein Aggregation Regulates Bacterial Dormancy Depth Critical for Antibiotic Tolerance, Mol. Cell 73 (2019) 143–156.
[60] A. Rajkovic, I. Tomasevic, B. De Meulenaer, F. Devlieghere, The effect of pulsed UV light on Escherichia coli O157:H7, Listeria monocytogenes, Salmonella Typhimurium, Staphylococcus aureus and staphylococcal enterotoxin A on sliced fermented salami and its chemical quality, Food Control 73 (2017) 829–837.
[61] W. Wang, X. Cheng, J. Liao, Z. Lin, L. Chen, D. Liu, T. Zhang, L. Li, Y. Lu, H. Xia, Synergistic photothermal and photodynamic therapy for effective implant-related bacterial infection elimination and biofilm disruption using Cu9S8 nanoparticles, ACS Biomater. Sci. Eng. 5 (2019) 6243–6253.
[62] W. Wang, Y. Yu, T. An, G. Li, H.Y. Yip, J.C. Yu, P.K. Wong, Visible-light-driven photocatalytic inactivation of E. coli K-12 by bismuth vanadate nanotubes: bactericidal performance and mechanism, Environ. Sci. Technol. 46 (2012) 4599–4606.
[63] D. Árus, A. Jancsó, D. Szunyogh, F. Matyuska, N.V. Nagy, E. Hoffmann, T. Körtvélyesi, T. Gajda, On the possible roles of N-terminal His-rich domains of Cu,Zn SODs of some Gram-negative bacteria, J. Inorg. Biochem. 106 (2012) 10–18.
[64] B. Shi, T. Wang, Z. Zeng, L. Zhou, W. You, C. Ke, The role of copper and zinc accumulation in defense against bacterial pathogen in the fujian oyster (Crassostrea angulata), Fish Shellfish Immunol. 92 (2019) 72–82.
[65] Z. Xikeranmu, M. Abdunasir, J. Ma, K. Tusong, X. Liu, Characterization of two copper/zinc superoxide dismutases (Cu/Zn-SODs) from the desert beetle Microdera punctipennis and their activities in protecting E. coli cells against cold, Cryobiology 87 (2019) 15–27.
[66] O. Clements Mark, P. Watson Sean, J. Foster, Simon, Characterization of the major superoxide dismutase of staphylococcus aureus and its role in starvation survival, stress resistance, and pathogenicity, J. Bacteriol. 181 (1999) 3898–3903.
[67] C.M. Hansel, J.M. Diaz, S. Plummer, Tight regulation of extracellular superoxide points to its vital role in the physiology of the globally relevant *Roseobacter* Clade, mBio 10 (2019), 02668-02618.
[68] R. Sinha, I. Sinha, A. Calcagnotto, N. Trushin, J.S. Haley, T.D. Schell, J.P. Richie, Oral supplementation with liposomal glutathione elevates body stores of glutathione and markers of immune function, Eur. J. Clin. Nutr. 72 (2018) 105–111.
[69] G. Wu, N. Li, Y. Mao, G. Zhou, H. Gao, Endogenous generation of hydrogen sulfide and its regulation in Shewanella oneidensis, Front. Microbiol. 6 (2015) 374.